NUCL SCI TECH (2020) 31:5
https://doi.org/10.1007/s41365-019-0721-0

Seismic and stress qualification of LMFR fuel rod and simple method for the determination of LBE added mass effect

M. Khizer[1,2] · Jian-Wei Chen[1] · Guo-Wei Yang[1,2] · Qing-Sheng Wu[1] · Yong Song[1] · Yong Zhang[1]

Received: 30 May 2019 / Revised: 19 November 2019 / Accepted: 21 November 2019 / Published online: 21 December 2019

Abstract In this study, two different designs of liquid metal fast reactor (LMFR) fuel rods wire-wrapped and non-wire-wrapped (bare) are compared with respect to different parameters as a means of considering the optimum fuel design. Nuclear seismic rules require that systems and components that are important for safety must be capable of bearing earthquake effects, and that their integrity and functionality should be guaranteed. Mode shapes, natural frequencies, stresses on cladding, and seismic aspects are considered for comparison using ANSYS. Modal analysis is compared in a vacuum and in lead–bismuth eutectic (LBE) using potential flow theory by considering the added mass effect. A simple and accurate approach is suggested for the determination of the LBE added mass effect and is verified by a manually calculated added mass, which further proved the usefulness of potential flow theory for the accurate estimation of the added mass effect. The verification of the hydrodynamic function (τ) over the entire frequency range further validated the finite element method (FEM) modal analysis results. Stresses obtained for fuel rods against different loading combinations revealed that they were within the allowable limits with maximum stress ratios of 0.25 (bare) and 0.74 (wire-wrapped). In order to verify the structural integrity of cladding tubes, stresses along the cladding length were determined during different transients and were also calculated manually for static pressure. The manual calculations could be roughly compared with the ANSYS results, and the two showed a close agreement. Contact analysis methodology was selected, and the most appropriate analysis options were suggested for establishing contact between the wire and cladding for the wire-wrapped design grid independence analysis, which proved the accuracy of the results, confirmed the selection of the appropriate procedure, and validated the use of the ANSYS mechanical APDL code for LMFR fuel rod analysis. The results provided detailed insight into the structural design of LMFR fuel rods by considering different structural configurations (i.e., bare and wire-wrapped) in the seismic loading; this not only provides a FEM procedure for LMFR fuel with complex configuration, but also guides the reference design of LMFR fuel rods.

Keywords LMFR · Fuel rod · Added mass · Seismic analysis · Contact analysis

This work was supported by the National Key R&D Program of China (No. 2018YFB1900601) and National Natural Science Foundation of China (No. 11772086)

✉ Jian-Wei Chen
jianwei.chen@fds.org.cn

[1] Key Laboratory of Neutronics and Radiation Safety, Institute of Nuclear, Energy Safety Technology, Chinese Academy of Sciences, Hefei 230031, China

[2] University of Science and Technology of China, Hefei 230027, China

1 Introduction

The Chinese Academy of Sciences (CAS) has launched an engineering program for nuclear transmutation by developing an accelerator-driven subcritical (ADS) system. The design proposed by the Institute of Nuclear Energy Safety Technology (INEST) was selected as the reference reactor [1–5]. Initially, the design of a 10 MW_{th} lead–bismuth-cooled research reactor was under consideration [6–10]. The ADS system is an advanced-stage nuclear energy system for the transmutation of long-lived radioactive waste and fission fuel breeding [8–14].

Nuclear fuel is the most critical and important component that bears safety Class III, ASME Class I, and seismic Class I code components. To accomplish the requirements laid down in the codes, seismic qualification of the fuel rod is mandatory with respect to operational basis earthquakes (OBEs) and safe shutdown earthquakes (SSEs). Researchers have studied the potential failures of fuel rod cladding and have shown that the mechanical failure of fuel rods encompasses cladding collapse, fatigue fracture, and rupture, and that these excessive stresses on cladding are usually caused by different operational transients during the lifetime of a plant [15]. The authors proposed the RODSIS rod design model, whereby the fuel rods were fastened using a stiff middle grid and softer end grids that were made of HT-9 due to high coolant density. Finite element analysis (FEA) was conducted using ANSYS for thermal and mechanical analyses of the middle grid only, and validated that for a peak power of the fuel rod, adequate margins exist against static stresses, fuel melting, clad oxidation, and fuel cladding chemical interaction (FCCI) without taking into consideration the seismic aspect. Another study highlighted the mechanical response, deformation, and bowing of wire-wrapped fuel rods and their effect on the wrapper by considering their neutronic and thermal environments for liquid metal fast breeder reactor (LMFBR) fuel assembly [3, 16, 17]. A sub-channel deformation analysis code (SHADOW) for wire-wrapped fuel assemblies was developed and applied to study the deformation due to thermal bowing of 169 fuel pins of a prototype fuel assembly of an LMFBR. This code was considered to be an effective tool for thermal and structural analysis of fuel assembly, but it lacks the capability to accommodate dynamic effects in the event of an earthquake event. The flow path of the coolant between the rods within the fuel assembly is maintained either by tightly wrapped thin wires around the rods or by grid spacers. The Fermi reactor in the USA and the demonstration and prototype plants in Germany and the UK used grid spacers, whereas a wire-wrapped design has been adopted for the fuel assembly design by other plants [18, 19], which focused on the computational fluid dynamics (CFD) analysis of a 19-pin, wire-wrapped, LBE-cooled fuel assembly of a GEN-IV research reactor. A CFD and sensitivity analysis model was developed to describe and validate the experimental test section [19]. This code was validated by the experimental data of a similar geometry cooled by sodium by considering only the heat transfer effects.

A steel wire of a usually circular cross section is welded to the extreme ends of cladding and wrapped around the cladding with a quantified axial pitch. The formerly used grid spacer design usually consists of a steel weblike structure containing rods, which is attached to the fuel assembly duct wall at designated axial levels depending upon the length of the assembly. Wire-wrapped designs are widely preferred for their several benefits, including that fabrication is easy and less expensive when compared to the grid spacer design that was usually employed in the previous generation of reactors [19]. Due to the use of wire-wrapped technology, contact with neighboring cladding occurs at six axial locations for every pitch of wire, which helps to minimize cladding mechanical vibrations. The grid design requires several grids to provide a similar structural stability, thus resulting in an unnecessary pressure drop. On the other hand, the added advantage of the wire-wrapped design is that it enables a better heat mixing of the coolant due to an increase in the local turbulence of the coolant.

Generally speaking, mostly of the studies that have been conducted so far in the research and development of LMFRs relate to heat transfer and fluid dynamics. To some extent, the literature exists regarding the justification of the seismic design of reactor components as a whole (fuel assembly or core), but is limited to individual fuel rods or a comparison between different designs of fuel rods. The present study highlights the comparison of two different designs of fuel rods that are under consideration for the CLEAR-I (China lead-based research reactor) and presents their qualification in detail by considering different loads (e.g., dead weight (DW)), design and operating pressures (DP, OP), earthquakes (as response spectrum), different plant conditions, and combinations of the aforesaid loads according to code requirements using ANSYS mechanical APDL code (ANSYS parametric design language). The present work deals with the seismic and stress analyses of the Class I component that should be confirmed "by analysis" instead of "by rules" [20, 21].

2 Structural design and modeling

The fuel rod comprised a 15-15Ti stainless steel cladding holding UO_2 pellets [22] enclosed by upper and lower end caps, along with reflectors, gas chambers, and a ballast for compensating the buoyancy caused by the high density of the LBE. Based on the CLEAR-I design, each fuel assembly consisted of 61 fuel rods [23, 24]. The two designs under consideration differed in geometry in terms of one having a tightly wrapped wire around cladding and being welded at extreme ends of the cladding. The remaining features of the two designs are completely identical. Figure 1 shows the schematic of two different fuel rod designs for the CLEAR-I.

The fuel rods in most LMFR's assemblies are separated by wire that is usually of a very small diameter, which is wrapped helically around the fuel rod cladding (wire spacers) along its axis. These wire-wrapped fuel rods were initially designed to maintain a constant gap among the fuel rods, but it was later found that they also provide additional turbulence and cause rotation of the liquid metal coolant within the assembly as it flows through the core [25]. In consideration of the service conditions and design load cases, the preliminary structural design parameters and material properties of fuel rods are listed in Tables 1 and 2.

During assembling, the pellets are piled within the cladding to the required height. A compressive spring is then installed on the top of the fuel column, and the upper and lower end plugs are inserted and welded onto the ends of the clad tube. In order to minimize clad stresses and clad flattening due to the coolant operating pressure, the fuel rod is internally pressurized with helium during the plug welding process. An initial rod pressure is selected to slow down the pellet–clad mechanical interaction and to avoid the probability of rod flattening.

Modeling of the wire around cladding requires special care and attention because the wire should remain in contact with the cladding along the whole length of the cladding. Wire surrounds the cladding in complete full 03 loops or turns. By choosing a correct angle and performing orientation calculations for modeling, the ANSYS model is able to attain the geometry that is closest to the actual geometry. The cladding was divided into equal numbers after exact calculations of wire turns and radius were performed. A helical path was made around the rod centerline according to the number of cladding divisions. A circular cross section equal to the wire diameter was created for the wire, which was away from and exactly equal to the radius of wire, on the bottom horizontal plane. This was then simplified radially to reduce the cell count followed by sweeping the cross section along the helical path. The purpose of the geometric estimation in this method is to keep the wire perfectly horizontal instead of normal to the helical path in order to resemble the real geometry because of the selection of the sweep path and the orientation of the plane on which the sweep sketch was made. By using accurate wire dimensions, this problem is hardly evident: The angle between the wire normal plane and the horizontal plane is smaller, so the variation in the sweep is considerably small and can therefore be ignored [26]. ANSYS 3-D models of both designs and wire are shown in Fig. 2.

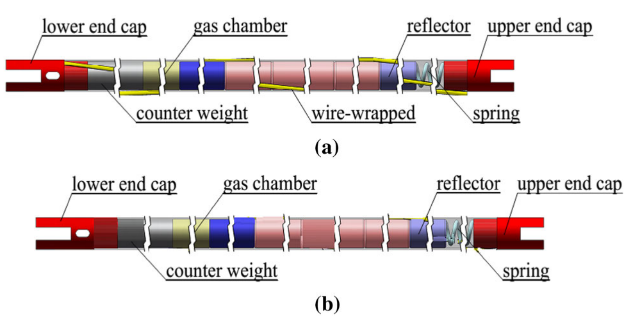

Fig. 1 (Color online) Schematic views of two different designs of the CLEAR-I. **a** Schematic view of the wire-wrapped fuel rod. **b** Schematic view of the bare design

Table 1 Technical parameters of two different designs of the CLEAR-I fuel rod

Component	Wire-wrapped	Bare
Total length (mm)	1675	1675
Cladding length (mm)	1630	1630
Cladding outside diameter (mm)	12	12
Cladding thickness (mm)	0.4	0.4
Total length of wire (mm)	1843.62	–
Diameter of wire (mm)	1.6	–
Number of loops	3	–

3 Methodology of analysis and assumptions

DP (0.9 and 3.75 MPa) and OP (0.6 and 2.5 MPa) were applied on the outside and inside areas of the cladding. Only plant operating conditions that involve seismic loadings were considered. Thus, the service levels with a loading combination other than seismic loads were overlooked, as listed in Table 3. Moreover, in the absence of nozzles, service levels B and C are the same.

3.1 Floor response spectrum

The US NRC RG 1.60 spectra were used as the site response spectrum. The design response spectra for SSEs were characterized by RG 1.60 spectra, where the horizontal component was scaled to a maximum ground acceleration of 0.3 g and the vertical component was scaled to a maximum ground acceleration of 0.217 g, which are considered to be fit for a typical site in China for an LMFR. The response spectra for horizontal and vertical components of OBEs were obtained by dividing the corresponding values of the SSE spectra by 2. Figure 3 shows the acceleration versus frequency curves for OBEs and SSEs. The spectrum amplification factors for SSEs and OBEs are all in accord with RG 1.60.

Since the fuel rods first-order natural frequencies (Table 4) are 8.07 Hz (bare) and 7.91 Hz (wire-wrapped),

Table 2 Material properties: S_u is the ultimate tensile strength, S_y is the yield strength, S_m is the stress intensity, E is the modulus of elasticity, and υ is Poisson's ratio

Component	Material	S_u (MPa)	S_y (MPa)	S_m (MPa)	E (MPa)	ρ (Kg/m^3)	υ (−)
Fuel rod	316L	360	149	120	1.65e5	7778	0.3
Wire	316L	360	149	120	1.65e5	7778	0.3

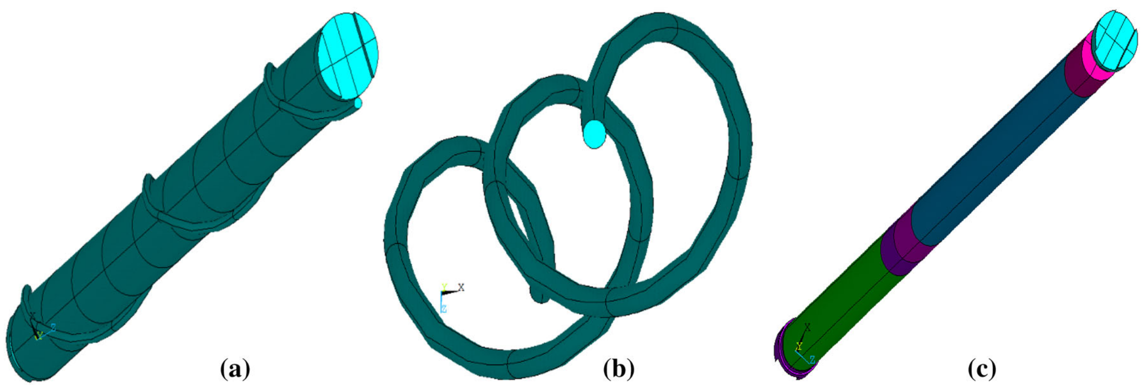

Fig. 2 (Color online) Three-dimensional models of fuel rods and wire. **a** 3-D model of the wire-wrapped design; **b** 3-D model of the wire; **c** 3-D model of the bare design

Table 3 Analysis types, load cases, and combinations

Service level	Operating condition	Load combination
Level 0	Design	DP + DW
Level A	Normal	OP + DW
Level B	Upset	OP + DW + OBE
Level D	Faulted	OP + DW + SSE

Table 4 Mesh details

Model type	Element type	Total elements	Total nodes
Bare	SOLID95	658,560	1,320,976
Wire-wrapped	SOLID95	1,178,846	2,282,429
Wire-wrapped	TARGE170	1,178,846	2,282,429
Wire-wrapped	CONTA174	1,178,846	2,282,429

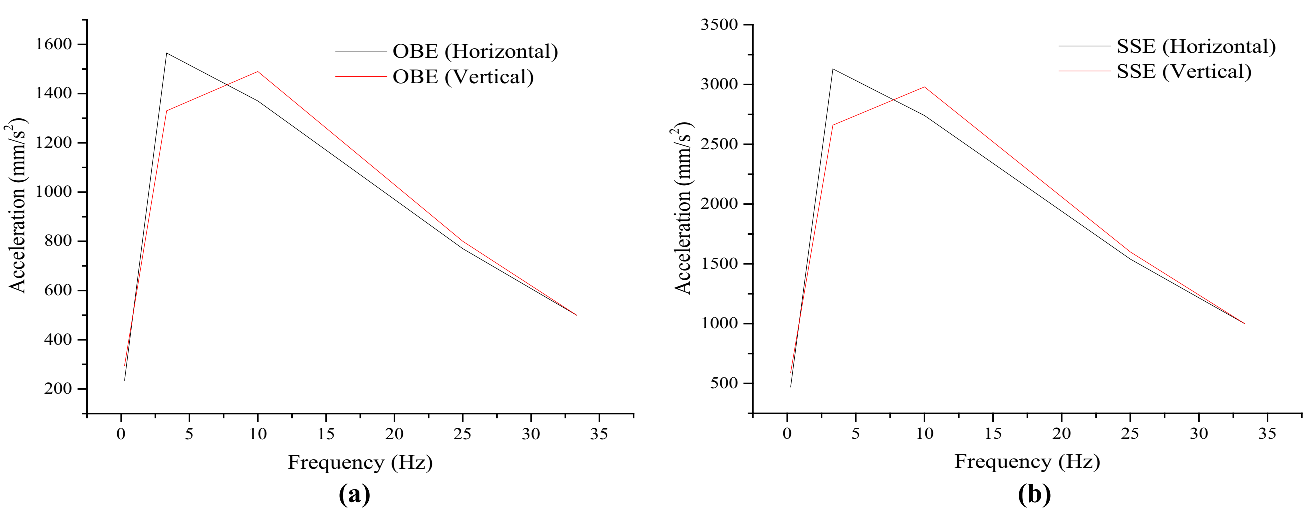

Fig. 3 (Color online) Horizontal and vertical response spectra for OBEs and SSEs **a** horizontal and vertical response spectra for OBEs; **b** horizontal and vertical response spectra for SSEs

they are less than the zero-period acceleration of 33 Hz; hence, the seismic calculation of the equivalent static method could not be applied. The FEM-based software ANSYS was used in this analysis. The methodology is presented in a flowchart in Fig. 4.

The following assumptions were made before undergoing any analysis:

The fluid (LBE) was viscous, incompressible, stationary, and Newtonian gravity effects were neglected. The rod bundle did not undergo any deformation, and the pitch between the rods remained constant in the fuel assembly. The effective density method was used for the analysis, which included the density of all integral components of the fuel rod to form a cumulative mass for the fuel rod. In a stationary fluid, added stiffness is typically quite small compared to the structural stiffness and can therefore be ignored. The model was then investigated by static (pressure and weight) and dynamic (OBE and SSE) analyses, whereby loads were applied and results were compared with the allowable limits defined by code.

3.2 Mesh detail and mesh independency study

After modeling in 3-D with the necessary details, the models were discretized with a higher-order 20-node 3-D solid element (SOLID95) to tolerate irregular configurations of geometry without loss of certainty. SOLID95 is compatible with displacement shapes and is appropriate for curved borders [27]. The type of elements used and the total number of elements and nodes used in this analysis are listed in Table 4, and the 3-D meshed view of the fuel rod and the wire is shown in Fig. 5.

The authenticity of the FEM results is based upon the convergence of solution, i.e., the results should become independent of the mesh or grid size. The grid independency procedure provides the basis for selecting the optimum mesh size for better and accurate results with minimal processing time. The meshed fuel rods (bare and wire-wrapped) were subjected to a calculated stress with three different meshed states:

(1) A coarse mesh of (0.262075, bare) and (1.923422, wire-wrapped) million total nodes;

(2) A medium mesh of (1.320976, bare) and (2.282429, wire-wrapped) million total nodes; and

(3) A fine mesh of (1.51195, bare) and (3.311429, wire-wrapped) million total nodes.

The analysis results revealed that the solution became independent of the mesh size for both models when the total number of nodes were (1.320976, bare) and (2.282429, wire-wrapped) million, as shown in Fig. 6, which plots the average stress intensity (S_{INT}) against the number of nodes.

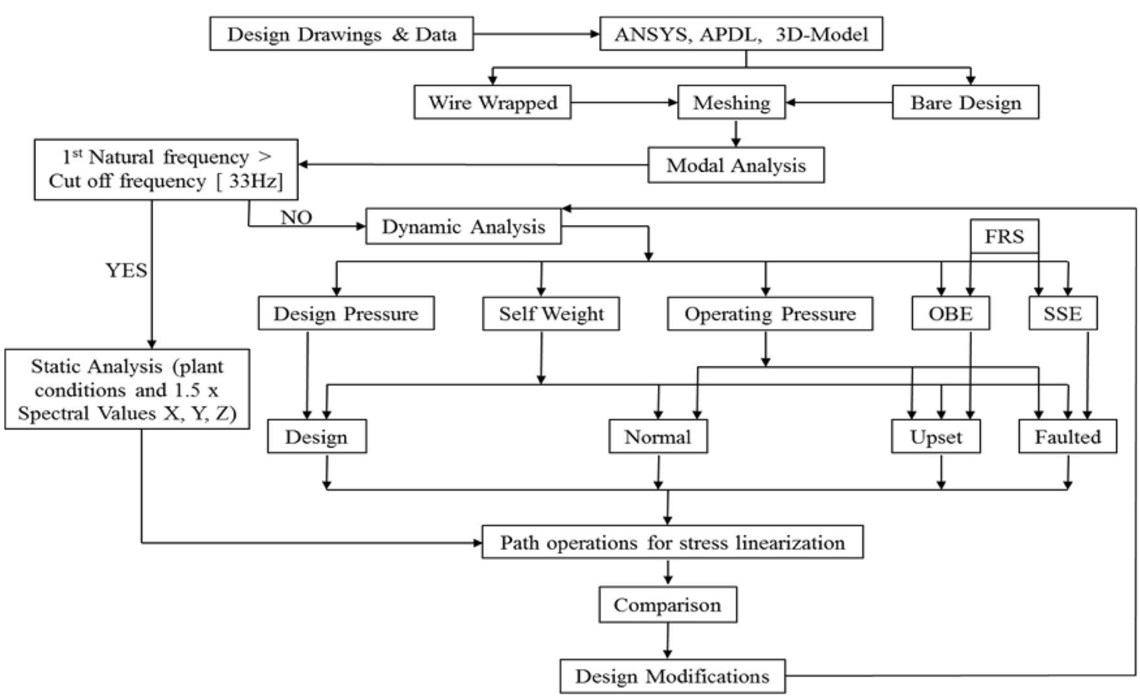

Fig. 4 Methodology of analysis

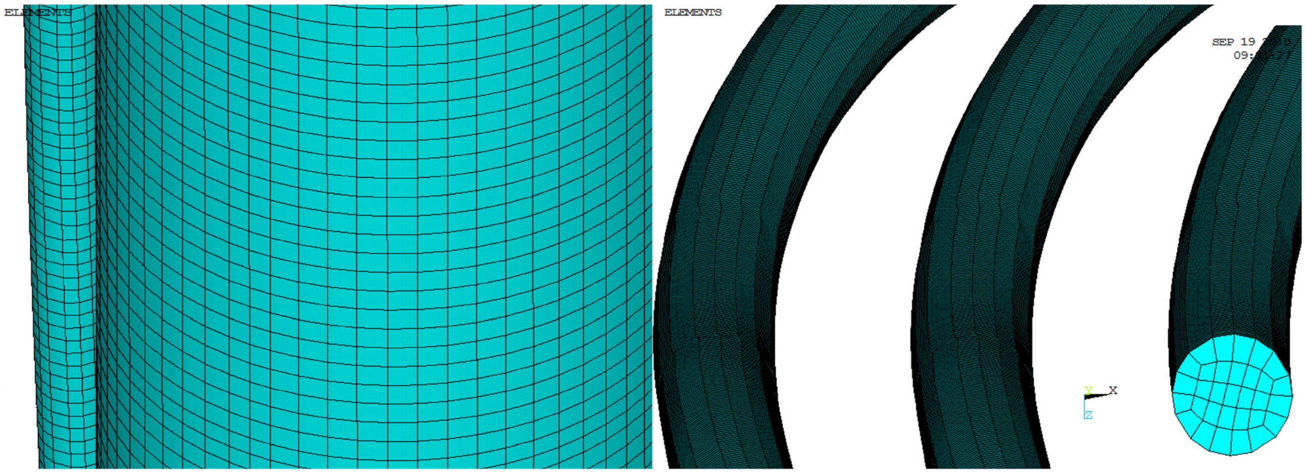

(a) (b)

Fig. 5 (Color online) Meshed models of the fuel rod and wire. **a** Meshed model of the wire-wrapped design; **b** meshed model of the wire

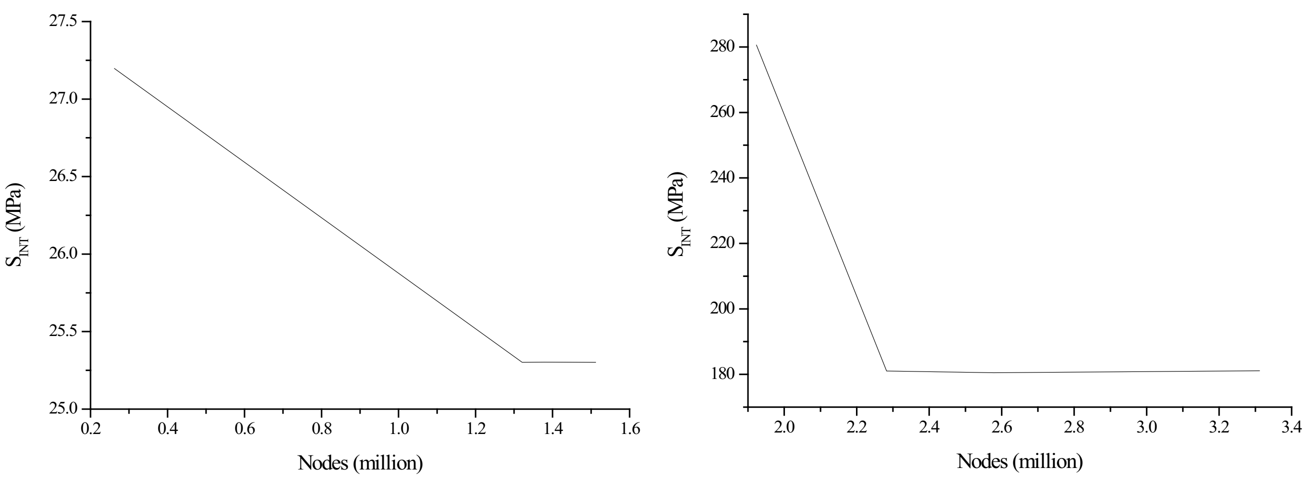

(a) (b)

Fig. 6 Mesh dependency. **a** Bare; **b** wire-wrapped

4 Contact analysis strategy for wire-wrapped design

ANSYS FEA has a huge library of elements. These elements range from those that are simple, complex, sophisticated, and of general purpose. Selection of the best choice of contact element and solution options can greatly affect the results and system performance. By considering the geometry of the cladding and by keeping in view the layout of the wire-wrapped around the cladding, surface-to-surface contact elements TARGE170 and CONTA174 are best suited to this analysis because they overcome most of the restrictions or limitations of other elements. This is due to the fact that 3-D systems with rigid or flexible target faces can be treated, sliding is permitted, higher-order solid (e.g., SOLID95) element faces are compatible, and stiffness can be assigned automatically for a closed gap. The software assigns default values of parameters for contact elements, but still provides the user with a selection of different options: stiffness of a closed gap (FKN), formulation methods (penalty method or penalty plus LaGrange multipliers), allowable penetration tolerance (FTOLN), pinball region size (PINB), friction/sliding behavior, and initial closure (ICONT). For this analysis, the default values assigned by the software were used.

4.1 Asymmetric pattern of contact elements

Asymmetric contact pattern defines the selection of target and contact surfaces and assigns all the contact elements on a contact surface and the target elements on a target surface. This is also called "one pass contact" and is the most efficient way of modeling surface-to-surface contact. ANSYS provides the following guidelines for defining the contact and target surfaces in a model for TARGE170/CONTA174 elements: If convex and flat or concave surfaces come into contact, the concave/flat surface would be the target surface. If fine and coarse mesh surfaces come into contact, the coarse mesh would be the target surface. If stiffer and softer surfaces come into contact, the stiffer surface would be the target surface. If surfaces with higher- and lower-order elements come into contact, the lower-order element surface would be the target surface. The general layout for surface-to-surface contact is shown in Fig. 7.

Keeping in view the aforementioned guidelines, the wire-wrapped around the cladding was treated as the target surface because the solid wire of 1.6 mm diameter was much stiffer and the cladding was treated as the contact surface in this analysis. The cladding surface was meshed with CONTA174 and the wire-wrapped surface was meshed with TARGE170 elements. While using the TARGE170/CONTA174 element pair meshing, the following elements from the KEYOPT and SOLUTION settings were considered after a detailed review of the available literature and the ANSYS guidelines to expedite the solution: KEYOPT,3,2,1, KEYOPT,3,6,0, KEYOPT,3,7,0, KEYOPT,3,8,1, KEYOPT,3,9,1, KEYOPT,3,11,0, KEYOPT,n,12,5; SOLCON, OFF, OFF, NSUBST, 1, 1, 1, NEQIT, 1, LNSRCH, OFF, NLGEOM, OFF.

"Always bonded" contact was found to be a very useful feature. The use of contact elements is quite ideal when compared to the constraint equations to connect different meshes because the contact element function is appropriate for large deformation problems, whereas the constraint equations are limited to small deformations.

5 Results and discussion

Since fuel pellets are not a solitary integral piece, they do not contribute during the bending moment. The fuel column was therefore divided into small pieces (pellets), which did not defy the bending of the fuel rod [25, 26]; hence, it can be fairly assumed that the pellets contributed only to the mass of the fuel rod and not to the stiffness, and that the mass per unit length collectively included the fuel and cladding [27]. The lower end cap was constrained in all degree of freedom (DOF), whereas the upper end cap was constrained in horizontal directions, thereby allowing room for thermal expansion of the fuel rod in the vertical direction.

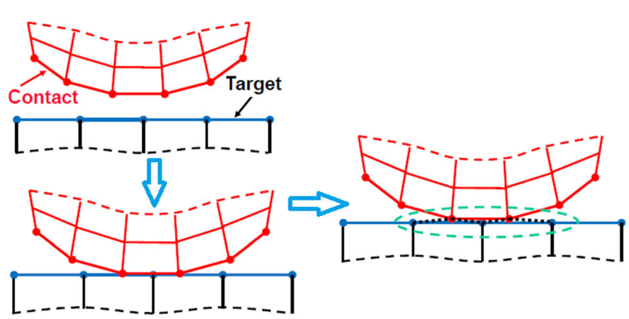

Fig. 7 (Color online) General layout of surface-to-surface contact

5.1 Modal analysis in a vacuum and in LBE

Modal analysis of the two designs was compared in a vacuum and in LBE by means of potential flow theory using the added mass effect (i.e., the mass of LBE displaced by the fuel rod volume). The added mass effect in the system due to LBE (higher density in comparison with the vacuum) was inversely proportional to the natural frequencies. The results obtained from the modal analysis showed very little difference in natural frequencies and mode shapes of the two designs. The wire-wrapped design showed a small lag in both mode shapes and natural frequencies in comparison with the bare design because of an increase in mass, as exhibited in Fig. 8.

Referring to recent numerical studies, the hydrodynamic functions (τ) for a circular cylinder and a thin rectangular beam are approximately identical. Furthermore, it has been reported that the hydrodynamic functions for a rectangular beam and a circular cylinder possess the same asymptotic forms, and the difference in the results never exceeds 15% over the entire frequency range [28].

$$\omega_{\mathrm{lbe}_{(n)}} = \omega_{\mathrm{vac}_{(n)}}\left[\left(1+\frac{\pi l \rho_{\mathrm{lbe}}}{4t\rho_{\mathrm{rod}}}\right)\tau_{(n)}\right]^{-1/2}, \tag{1}$$

where ω_{lbe} and ω_{vac} are frequencies in LBE and the vacuum, ρ_{lbe} and ρ_{rod} are densities of LBE and the rod, and l and t are the length and thickness of the fuel rod. Substituting values gives a constant hydrodynamic function (τ) over the entire frequency range, which further validates the FEM modal analysis results. The vacuum and LBE frequency comparison results for the verification of the hydrodynamic function are listed in Table 5.

5.2 Verification of LBE added mass effect for natural frequencies

The calculation of the added mass effect generally involves varying engineering judgments regarding the considerations of geometry, adjacent members, and certain irregularities among others. These factors vary significantly from one situation to another, and in some cases, a preliminary analysis must be performed. The potential flow theory accurately provides the added mass effect values.

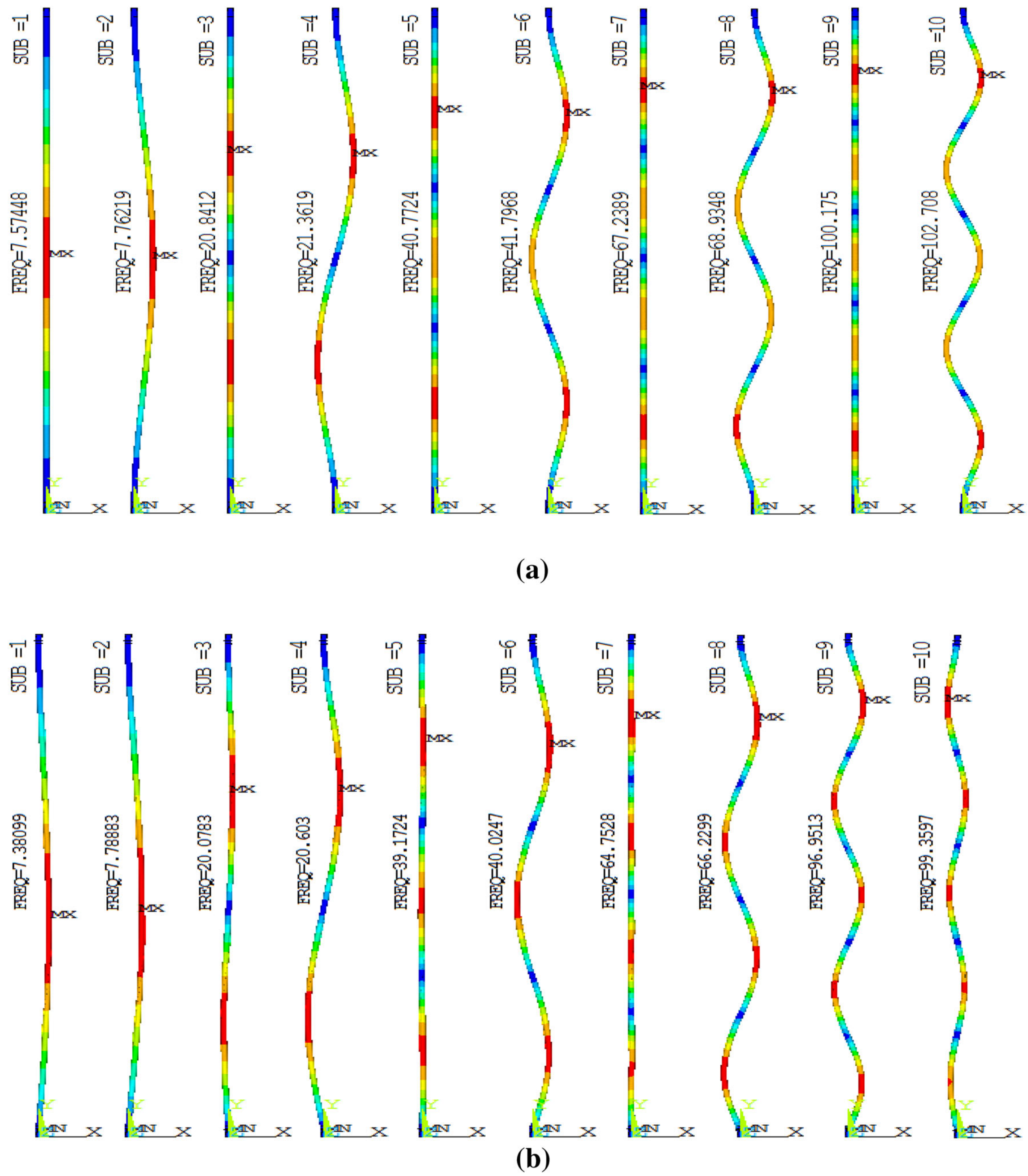

Fig. 8 (Color online) Mode shape comparison of the two designs in LBE: **a** bare; **b** wire-wrapped

The effect of added mass for single isolated members has been thoroughly investigated both analytically and experimentally. Theoretically, the potential flow theory has been quite successful for determining the added mass effect. The natural frequency of a component or structure submerged in, or in contact with, a fluid decreases considerably in comparison with that in a vacuum. This phenomenon is termed the fluid–structure interaction (FSI). A lot of work has been undertaken to find the approximate solutions for determining the added mass effect in order to approximately calculate the change in the natural frequency of a solid body vibrating in a liquid [29].

When a cylinder vibrates in a liquid, it induces an acceleration in the liquid, which in turn produces a force on the cylinder. This extra force can be fairly assumed as the mass of fluid displaced, which can be approximated as being equal to the volume of the cylinder using potential flow theory. In order to determine the natural frequencies of a cylinder vibrating in a liquid, the solution of stiffness and mass matrices have to be obtained using high-level

Table 5 Natural frequency comparison of two designs in a vacuum and in LBE and hydrodynamic function verification

Medium	Design	Mode	1st	2nd	3rd	4th	5th	6th	7th	8th	9th	10th
Vacuum	Bare	Frequency (Hz)	8.07	8.27	22.2	22.76	43.44	44.53	71.63	73.44	106.73	109.43
	Wire-wrapped	Frequency (Hz)	7.91	8.35	21.53	22.09	42.01	42.93	69.45	71.03	103.99	106.57
LBE	Bare	Frequency (Hz)	7.57	7.76	20.84	21.36	40.77	41.79	67.23	68.93	100.18	102.71
	Wire-wrapped	Frequency (Hz)	7.38	7.78	20.07	20.6	39.17	40.02	64.75	66.23	96.95	99.36
Hydrodynamic function (τ)	Bare	9e−4	9e−4	9e−4	9e−4	9e−4	9e−4	9e−4	9e−4	9e−4	9e−4	
Hydrodynamic function (τ)	Wire−wrapped	1e−3	1e−3	1e−3	1e−3	1e−3	1e−3	1e−3	1e−3	1e−3	1e−3	

computer resources [30]. On the other hand, for a cylinder of uniform thickness, the reverse calculations (presented later in this section) would be time-saving and accurate, and could be verified manually by existing research. To support the previous statements, the volume of the cylinder was calculated manually and then verified through software computation; the mass of the fluid was calculated later by assuming an equal amount of fluid volume displaced by the cylinder. Furthermore, the natural frequencies of the cylinder were then calculated in a vacuum and in fluid. Subsequently, the derivation presented below was used to verify the added mass over the entire calculated frequency range. The uniform added mass can therefore be obtained to show the validity of this reverse method for any order of natural frequencies.

The dynamic equation of motion can be written as follows:

$$m\frac{\mathrm{d}^2\omega}{\mathrm{d}t^2} + k\omega = 0, \tag{2}$$

where m and k are the mass and stiffness of cylinder, respectively. Natural frequency in a vacuum, ω_{vac}, is given as:

$$\omega_{\mathrm{vac}_{(n)}} = 2\pi f_{\mathrm{vac}} = \sqrt{\frac{k}{m}}. \tag{3}$$

When the body is immersed in a fluid, the corresponding equation of motion due to the added mass effect of the liquid can be written as follows:

$$(m + m_{\mathrm{add}})\frac{\mathrm{d}^2\omega}{\mathrm{d}t^2} + k\omega = 0, \tag{4}$$

where m_{add} is the added mass of the fluid. Furthermore, the natural frequency of the structure vibrating in a fluid can be expressed as:

$$\omega_{\mathrm{lbe}} = 2\pi f_{\mathrm{lbe}} = \sqrt{\frac{k}{m + m_{\mathrm{add}}}}. \tag{5}$$

Comparing Eqs. (3) and (5), we get the natural frequency as:

$$\frac{\omega_{\mathrm{lbe}}}{\omega_{\mathrm{vac}}} = \frac{f_{\mathrm{lbe}}}{f_{\mathrm{vac}}} = \sqrt{\frac{m}{m + m_{\mathrm{add}}}}, \tag{6}$$

$$\frac{f_{\mathrm{lbe}}}{f_{\mathrm{vac}}} = \sqrt{\frac{1}{1 + (m_{\mathrm{add}}/m)}}. \tag{7}$$

Since the term m_{add}/m in Eq. (7) is greater than zero, the non-dimensional frequency, $\omega_{\mathrm{lbe}}/\omega_{\mathrm{vac}}$, is always less than unity. This indicates how the liquid reduces the natural frequency. It is evident that the dynamic behavior is dependent upon the added mass for a single rigid body in an ideal fluid.

The manually calculated volume and volume obtained from FEM were approximately identical; the mass of the rod was calculated to be about $\sim$ 2054.4 g (bare) and 2083.03 g (wire-wrapped), and the calculated added mass (m_{cal}) of the LBE was approximated to be $\sim$ 277.1 g (bare) and 314.44 g (wire-wrapped). The frequencies were then calculated by using this added mass effect for an LBE environment. Equation (7) can be rewritten in the following form for the calculation of the added mass effect:

$$m_{\mathrm{add}} = m\left[\left(\frac{fn_{\mathrm{vac}}}{fn_{\mathrm{lbe}}}\right)^2 - 1\right], \tag{8}$$

where fn_{vac} and fn_{lbe} are the nth-order natural frequencies of the rod in a vacuum and in LBE, respectively. By substituting frequencies values from Table 5, a constant and uniform added mass of LBE was found over the entire frequency range, as presented in Table 6. Hence, for simple geometries, the added mass effect for single isolated members can be easily predicted with great accuracy.

Table 6 Verification of the added mass of LBE

Design	Mode	1st	2nd	3rd	4th	5th	6th	7th	8th	9th	10th
Bare	m_{add}	280.35	278.911	276.886	278.129	277.894	278.229	277.708	277.628	277.425	277.621
	m_{cal}	277.104	277.104	277.104	277.104	277.104	277.104	277.104	277.104	277.104	277.104
	% Diff	1.17	0.65	0.07	0.36	0.28	0.4	0.21	0.18	0.11	0.18
Wire-wrapped	m_{add}	309.932	316.407	314.085	312.23	313.009	313.943	313.377	312.876	313.501	313.277
	m_{cal}	314.442	314.44	314.44	314.44	314.44	314.44	314.44	314.44	314.44	314.44
	% Diff	1.43	0.62	0.11	0.7	0.45	0.15	0.33	0.49	0.29	0.37

5.3 Stress distribution and evaluation of results

The maximum stressed nodes, as sorted for ease of understanding the results, provide a comparison for the two different designs of LMFR fuel rods for different plant conditions. The stress distribution or stress contours have been compared along the most stressed nodes of the fuel rods at different loading conditions. As shown in Fig. 9, the most stressed nodes for the bare design are at the joint of the cladding with the end caps or cladding plugs, whereas they are at the extreme welding ends for the wire-wrapped design due to the discontinuity in geometry (i.e., the connection of the wire with the cladding). The contours were elaborated in terms of stress intensity (i.e., twice the maximum shear stress), which was defined as the difference between the algebraically largest and smallest principal stresses at a given position. To evaluate the results, the calculated stresses were compared with the allowable stress limits defined by the code, which showed that they were within the allowable limits.

Stress classification was performed to identify the “primary” (P) and “secondary” (Q) stresses. Primary stresses relate to equilibrium equations, while secondary stresses are linked to compatibility equations. In general, these stresses come from mechanical and thermal loadings, respectively. The integrity of the cladding is of the main concern of this study because it is the thinnest and longest section and bears all the mechanical loads. In the FEM, when continuum elements are used, the total stress distribution is obtained. Therefore, to calculate the membrane (P_m) and bending stresses (P_b), the stress distribution should be linearized across the thickness [27]. To check the stress limits and gain a better understanding of the behavior of the cladding for the two different designs, paths were defined along the full length of the cladding. The selection of the same path distance was considered for both models in order to get a true picture of the results. The stresses were then linearized and compared with the allowable limits [31]. For ease of understanding and for simplification, only four paths (the lowest and uppermost, and middle two paths of cladding) were selected and the ratio was also determined between calculated and allowable stress, for $P_m + P_b$ whichever is maximum (inside, center and outside of the cladding), listed in Table 7.

A graphical comparison was prepared to provide a better understanding of the two designs for different plant conditions (Fig. 10). Twenty paths were selected on the full length of the cladding by bearing in mind the same path distance for the two models in order to make a clear and true comparison between the two designs. It is interesting to note that the behavior of the two models for different plant conditions was opposite to each other at the beginning of the cladding length (0 mm distance) because of the discontinuity in geometry due to the attached wire. In structural discontinuity, there is an obvious increase in stress that can be observed due to the compatibility between linking parts. For the remaining length of the cladding, both models behaved in almost the same way for different loading combinations. The stresses remained uniform throughout the cladding length except for a small difference between the two models at the top section of the cladding (Fig. 10).

6 Analytical solution for static pressure

The prime concern in relation to the fuel rod is cladding. For the static analytical solution, the cladding can be treated as a thin cylinder since it satisfies the following laws of thin and thick cylinders:

$$\mathrm{od} > 10t \text{ or } \mathrm{id}/t > 20,$$

where od is the outside diameter, t is the thickness, and id is the inside diameter of the cladding. When $r_o = 6$ mm, $t = 0.4$ mm, and id = 11.6 mm, the criteria that the cladding could be treated as a thin cylinder are satisfied.

The method for determining the hoop or tangential stresses (δ_t), which are considered to be uniform throughout the wall thickness, and the radial stresses (δ_r), which are insignificant in comparison with the hoop stress, at any thickness of a cylinder against the applied pressure was presented by the French electrician Gabriel Lame in

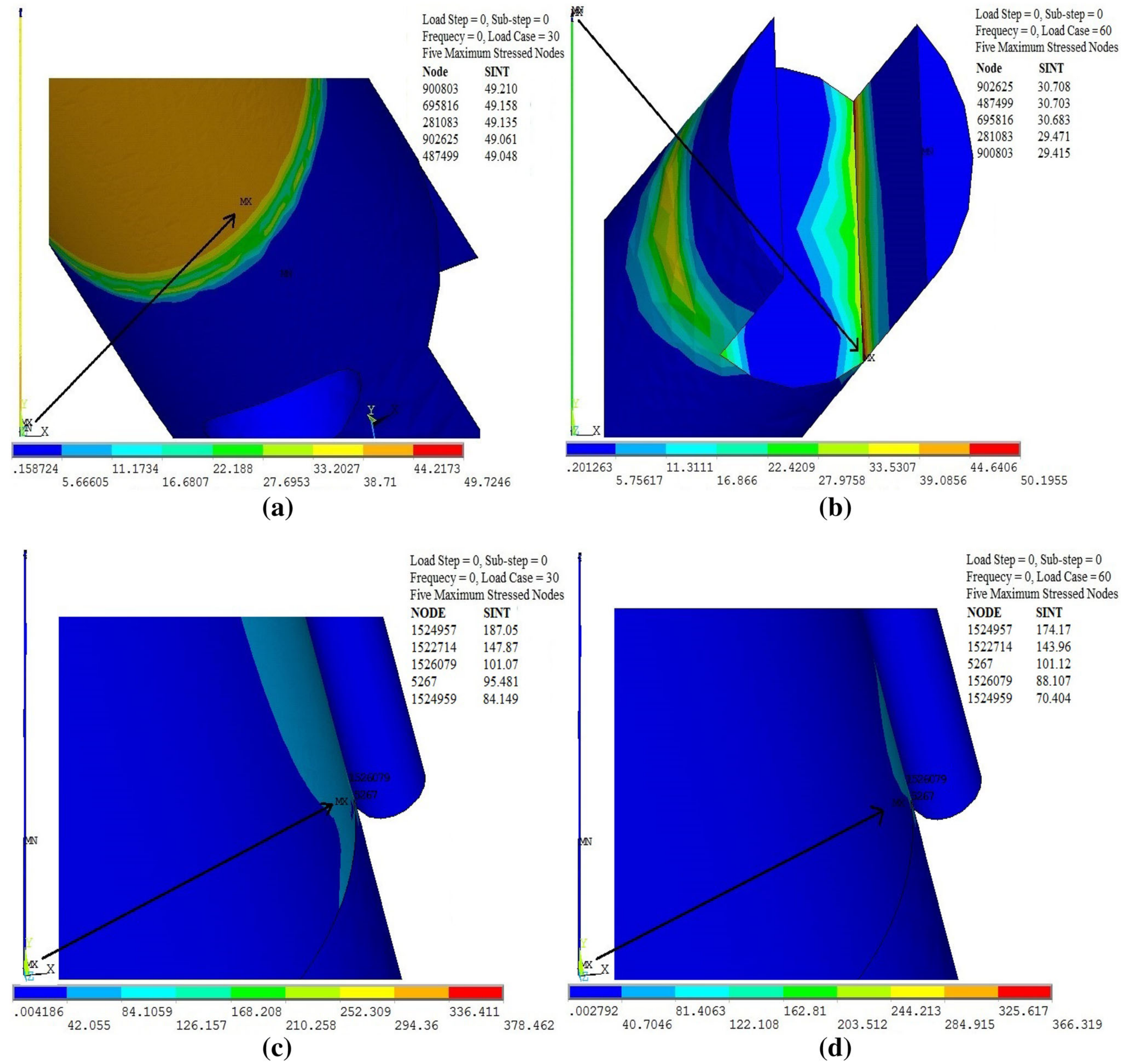

Fig. 9 (Color online) Stress intensity contour comparison of two designs for different plant conditions. **a** Design condition (bare); **b** faulted condition (bare); **c** design condition (wire-wrapped); **d** faulted condition (wire-wrapped)

(1833). This applies to a cylinder with a given inside radius (r_i) and outside radius (r_o) subjected to a uniformly distributed internal (P_i) and external pressure (P_o) [32].

When considering a thin shell of the radius (r) for the thickness (dr), the tangential stress in this shell is δ_t, the radial stress on the inner surface is δ_r, and that on the outer surface is $\delta_r + d\delta_r$, where $d\delta_r$ is the increment in δ_r due to the variation of pressure across the cylinder wall. The radial stresses are assumed to be tensile, so a negative result for δ_r will denote compression. Hence, for equilibrium, the vertical summation of forces must be zero:

$$(\delta_r + d\delta_r) \times 2(r + dr) - \delta_r(2r) - 2\delta_t dr = 0. \tag{9}$$

The final equation obtained from solving Eq. (9) gives the following general expression for δ_t and δ_r at any point:

$$\delta_t = \frac{r_i^2 P_i - r_o^2 P_o}{r_o^2 - r_i^2} + \frac{r_i^2 r_o^2 (P_i - P_o)}{\left(r_o^2 - r_i^2\right) r^2} \tag{10}$$

$$\delta_r = \frac{r_i^2 P_i - r_o^2 P_o}{r_o^2 - r_i^2} - \frac{r_i^2 r_o^2 (P_i - P_o)}{\left(r_o^2 - r_i^2\right) r^2}. \tag{11}$$

Substituting values for all variables and different values for "r" against the design and operating pressures in

Table 7 Stress evaluation comparison of fuel rod cladding under different plant conditions

Service level/allowable stress	Distance (mm)	Path	Bare				Wire-wrapped			
			Calculated stress (MPa)			Ratio	Calculated stress (MPa)			Ratio
			$P_m + P_b$				$P_m + P_b$			
			Inside	Center	Outside		Inside	Center	Outside	
Design ($1.5S_m = 180$)	0	1	1.39	1.33	1.27	0.008	79.16	106.4	133.8	0.74
	510	7	38.8	41.45	44.3	0.25	39.94	41.36	44.19	0.24
	1105	14	38.69	41.44	44.29	0.25	38.88	41.36	43.98	0.24
	1630	20	22.76	15.55	10.51	0.13	13.1	8.4	7.49	0.07
Normal ($3S_m = 360$)	0	1	0.81	0.77	0.74	0.002	69.02	97.14	125.5	0.35
	510	7	26.07	27.63	29.54	0.08	27.39	28.29	29.46	0.08
	1105	14	25.82	27.63	29.53	0.08	25.94	27.57	29.33	0.08
	1630	20	15.21	10.41	7.01	0.04	8.42	5.61	4.67	0.02
Upset ($3S_m = 360$)	0	1	2.8	2.69	2.59	0.008	104.5	103.9	115.2	0.32
	510	7	25.77	27.63	29.53	0.08	25.69	27.57	29.46	0.08
	1105	14	25.74	27.63	29.52	0.08	25.85	27.57	29.32	0.08
	1630	20	9.04	4.83	7.22	0.02	17.81	23.56	30.57	0.08
Faulted ($3.6S_m = 432$)	0	1	1.96	1.95	1.93	0.004	71.34	101.5	132.1	0.3
	510	7	26.08	27.63	29.54	0.07	27.03	27.93	29.46	0.06
	1105	14	25.82	27.63	29.53	0.07	25.91	27.57	29.32	0.06
	1630	20	15.22	10.44	7.02	0.03	13.23	11.34	10.47	0.03

Eq. (10), we obtain the following results in comparison with the ANSYS calculations (Table 8). The results were roughly compared with the ANSYS exact calculations and the two showed a close agreement.

It should be mentioned that for thin-walled cylinders, radial stresses are usually neglected because they are negligibly small. Due to internal pressure, the deformation of the cladding takes place, which results in stresses in the cladding wall. Each wall element is subjected to circular and axial expansion and radial compression that is governed by Eqs. (12) and (13). The inside wall deformation at $r = r_i$ is given as:

$$\Delta r_i = \frac{r_i}{E}\left[(P_i - P_o)\frac{r_o^2 + r_i^2}{r_o^2 - r_i^2} + v\right]. \tag{12}$$

The outside wall deformation at $r = r_o$ is expressed as:

$$\Delta r_o = \frac{r_o}{E}\left[(P_i - P_o)\frac{2r_i^2}{r_o^2 - r_i^2}\right]. \tag{13}$$

By substituting values into Eqs. (12) and (13), we obtain an estimated inside wall deformation $\Delta r_i = 0.00157\,\mathrm{mm}$ and an outside wall deformation $\Delta r_o = 0.00135\,\mathrm{mm}$.

7 Conclusion

A comparison of two different designs of lead-based reactor fuel rods was established for different plant conditions. ANSYS contact analysis methodology was developed for the wire-wrapped design, and most appropriate KEYOPT and SOLUTION settings were suggested. A simple yet accurate method for the determination and verification of the added mass effect was presented and verified using a manually calculation to show the usefulness of the potential flow theory for simple geometries. Modal frequencies were compared in a vacuum and in LBE, and a constant hydrodynamic function (τ) validated the FEM results. The use of wrapped wire provided thermal mixing of the coolant due to increased local turbulence in the coolant flow, although this resulted in high stress ratios on the extreme welded locations of the cladding. In comparison with the bare design, the wire-wrapped design yielded better stress results, but with some compromise in other aspects. Wire-wrapped designs are widely preferred due to several benefits including the fact that fabrication is easy and less expensive when compared to the grid spacer design that was usually employed in the previous generation of reactors. Secondly, due to the use of wire-wrapped technology, the contact with neighboring cladding occurred at six axial locations for every pitch of wire, which helped to minimize cladding mechanical vibrations and reactivity

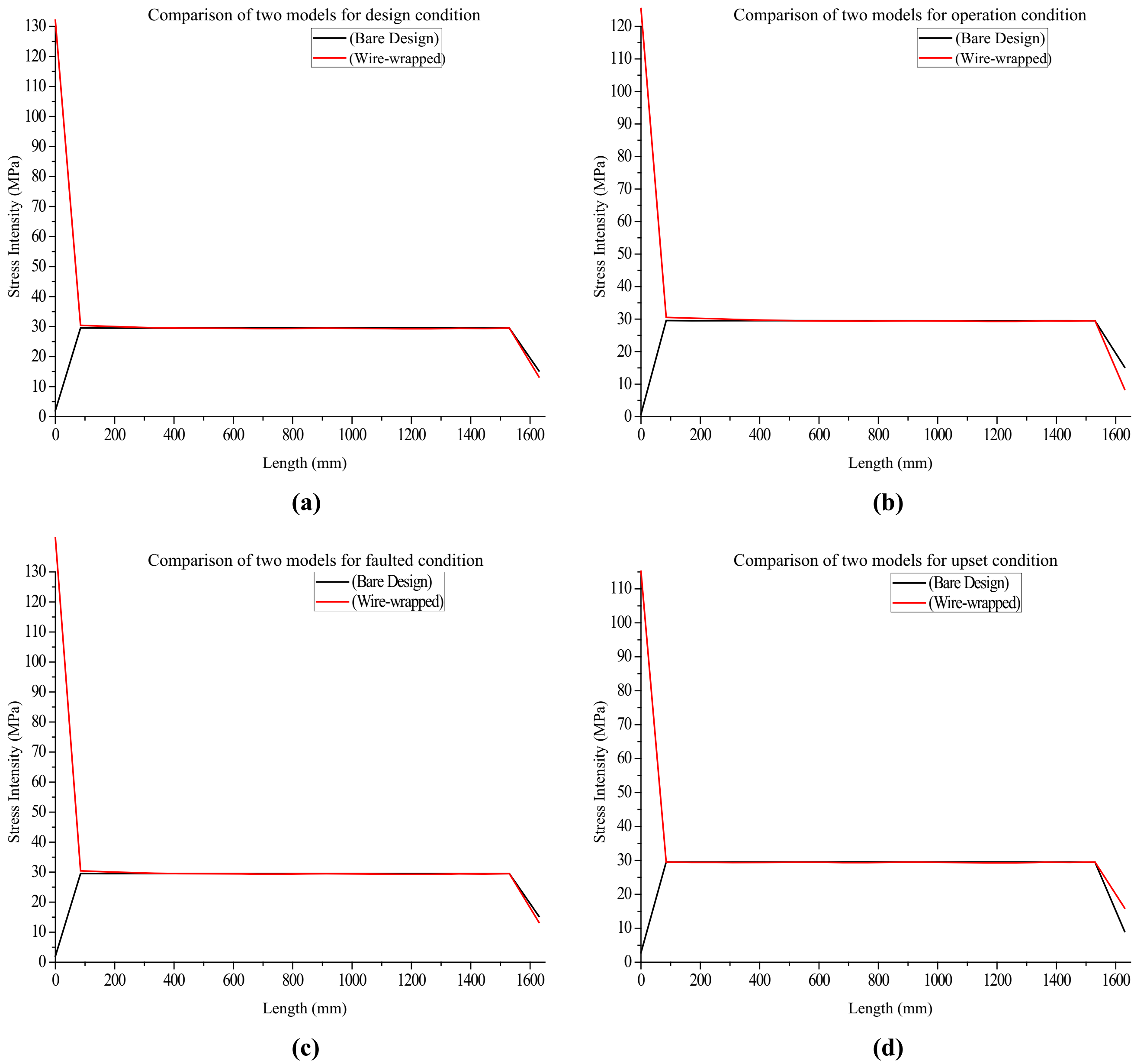

Fig. 10 (Color online) Stress distribution comparison of two designs along the cladding length for design and faulted conditions. **a** Design condition; **b** operation condition; **c** upset condition; **d** faulted condition

Table 8 Comparison of manual calculations and the ANSYS results

Designs	Radius (mm)	Design condition			Normal operation		
		ANSYS (MPa)	Manual (MPa)	% Diff	ANSYS (MPa)	Manual (MPa)	% Diff
Bare	5.6 (I)	38.8	40.47	4.12	26.07	26.98	3.37
	5.8 (C)	41.45	38.97	5.98	27.63	25.98	5.97
	6 (O)	44.3	37.62	15.07	29.54	25.08	15.09
Wire-wrapped	5.6 (I)	39.94	40.47	1.3	27.39	26.98	1.49
	5.8 (C)	41.36	38.97	5.77	28.29	25.98	8.16
	6 (O)	44.19	37.62	14.86	29.46	25.08	14.86

oscillations. Furthermore, the results were verified numerically and provided a close approximation to the ANSYS results. A mesh dependency test was also performed to determine the accuracy of the meshed model and to further validate the use of the APDL code for LMFR fuel rods analysis. The stresses remained uniform throughout the cladding length with a small difference at the top section of the cladding. The maximum stress ratios of 0.25 (bare) and 0.74 (wire-wrapped) that were computed on the cladding of the fuel rods in terms of the design condition were within the allowable limits defined by code. Hence, it is concluded that both fuel rod designs are adequate to bear the anticipated loads and will perform functions in all plant conditions. These results provide detailed insight into the design of LMFR fuel rods in consideration of different technical aspects and provide guidelines for further analysis.

Acknowledgements The authors are grateful to other members of the FDS Team for their great help in this research.

References

1. Y. Wu, Design and R&D progress of China lead-based reactor for ADS research facility. J. Eng. **2**, 124–131 (2016). https://doi.org/10.1016/J.ENG.2016.01.023
2. H. Shi, H. Ouyang, S. Wang et al., RF tuning and beam commissioning of CW RFQ for China-ADS Injector-I. Nucl. Sci. Tech. **29**, 142 (2018). https://doi.org/10.1007/s41365-018-0478-x
3. Z.L. Zhao, Y.W. Yang, H.Y. Meng et al., Preparation and verification of mixed high-energy neutron cross-section library for ADS. Nucl. Sci. Tech. **29**, 140 (2018). https://doi.org/10.1007/s41365-018-0487-9
4. Y. Wu, Y. Bai, Y. Song et al., Development strategy and conceptual design of China lead based research reactor. Ann. Nucl. Energy **87**, 511–516 (2016). https://doi.org/10.1016/J.ENG.2016.01.023
5. Y. Wu, J.P. Qian, J.N. Yu, The fusion-driven hybrid system and its material selection. J. Nucl. Math. **3**, 1629–1636 (2002). https://doi.org/10.1016/S0022-3115(02)01272-2
6. Y. Wu, Y. Bai, Y. Song et al., Conceptual design of China lead based research reactor CLEAR-1. Nucl. Sci. Eng. **34**, 201–208 (2014). https://doi.org/10.3969/j.issn.0258-0918.2014.02.009
7. Y. Wu, M.H. Wang, Q. Huang et al., Development status and prospects of lead-based reactors. Nucl. Sci. Eng. **35**, 213–221 (2015). https://doi.org/CNKI:SUN:HKXY.0.2015-02-004
8. M. Wang, C. Lian, Y. Li et al., Preliminary conceptual design of a lead-bismuth cooled small reactor (CLEAR-SR). Int. J. Hydrog. Energy. **40**(44), 15132–15136 (2015). https://doi.org/10.1016/j.ijhydene.2015.03.097
9. M. Zeng, Y. Song, X. Ding, Kinematics analysis and verification of in-vessel fuel handling system for China lead based research reactor. Ann. Nucl. Energ. **85**, 301–305 (2015). https://doi.org/10.1016/j.anucene.2015.05.031
10. Q. Han, Q. Wu, J. Chen et al., Analysis of fixation method of fuel assembly for lead alloy cooled reactor. Nucl. Sci. Tech. **26**, 050601 (2015). https://doi.org/10.13538/j.1001-8042/nst.26.050601
11. Y. Wu, F.D.S. Team, CLEAR-S: An integrated non-nuclear test facility for China lead based research reactor. Int. J. Energy Res. **40**(14), 1951–1956 (2016). https://doi.org/10.1002/er.3569
12. Y. Wu, S. Zheng, X. Zhu et al., Conceptual design of the fusion driven subcritical system FDS-I. Fus. Eng. Des. **81**, 1305–1311 (2006). https://doi.org/10.1016/j.fusengdes.2005.10.015
13. M. Barzegari, M. Aghaie, A. Zolfaghari, Assessment of fuel-rod meltdown in a severe accident at Bushehr nuclear power plant (BNPP). Nucl. Sci. Tech. **30**, 55 (2019). https://doi.org/10.1007/s41365-019-0589-z
14. K.L. Shi, S.Z. Li, X.L. Zhang et al., Partial flow blockage analysis of the hottest fuel assembly in SNCLFR-100 reactor core. Nucl. Sci. Tech. **29**, 16 (2018). https://doi.org/10.1007/s41365-017-0351-3
15. W.C. Nam, H.W. Lee, S. Hwang, Fuel design study and optimization for PEACER development. Nucl. Eng. Des. **237**, 316–324 (2007). https://doi.org/10.1016/j.nucengdes.2006.04.032
16. A.E. Aboanber, A.A. Nahla, A.M. Edress, Developed mathematical technique for fractional stochastic point kinetics model in nuclear reactor dynamics. Nucl. Sci. Tech. **29**, 132 (2018). https://doi.org/10.1007/s41365-018-0467-0
17. K. MiKi, Analytical method of fuel pin deformations in LMFBR assembly. J. Nucl. Sci. Technol. **14**(11), 791–804 (1977). https://doi.org/10.1080/18811248.1977.9730840
18. X. Yang, Y.T. Gao, Y. Zhong et al., Stress analysis of the TMSR graphite component under irradiation conditions. Nucl. Sci. Tech. **29**, 173 (2018). https://doi.org/10.1007/s41365-018-0516-8
19. R. Marinari, D. Piazza, CFD Pre-test analysis of the rod bundle experiment in the HLM facility NACIE-UP. ENEA, ADPFISS-LP2–110 (2015). doi:/nureth-16/data/papers/13290.pdf
20. H. S. Kang, K. N. Song, H. K. Kim et al., Modal analysis of a PWR fuel rod supported by the newly designed spacer grid. Transaction, SMiRT-16 (2001). doi:/1840.20/30513/C1425.pdf
21. R.L. Frano, A. Sanfiorenzo, G. Forasassi et al., Structural dynamic evaluation of the effects caused by the core compaction. CERSE-UNIPI RL **1**(12), 16154 (2014)
22. G. Grasso, C. Petrovich, D. Mattiol et al., The core design of ALFRED, a demonstrator for the European lead cooled reactors. Nucl. Eng. Des. **278**, 287–301 (2014). https://doi.org/10.1016/j.nucengdes.2014.07.032
23. Y. Wu, F.D.S. Team, Conceptual design of China fusion power plant FDS-II. Fus. Eng. Des. **83**, 1683–1689 (2008). https://doi.org/10.1016/j.fusengdes.2008.06.048
24. Y. Wu, Z. Chen, L. Hu et al., Identification of safety gaps for fusion demonstration reactors. Nat. Energy **1**(12), 16154 (2016). https://doi.org/10.1038/nenergy.2016.154
25. A. Shams, F. Roelofs, E. Baglietto et al., High-fidelity numerical simulations of an infinite wire wrapped fuel assembly. NURETH-16 (2015). https://doi.org/10.1016/j.nucengdes.2018.06.012
26. E. Sosnovsky, E. Baglietto, S. Keijers et al., CFD simulations to determine the effects of deformations on liquid metal cooled wire wrapped fuel assemblies, in *NURETH-16*, pp. 2747–2761 (2015). http://glc.ans.org/nureth-16/data/papers/13595.pdf
27. S. Hussain, M. Rafique, A. Ahmad et al., CNPP fuel rod vibration analysis using finite element method. Technical Journal, University of Engineering and Technology Taxila, Vibration analysis issue, pp. 23–33 (2012)
28. E.O. Tuck, Calculation of unsteady flows due to small motion of cylinders in a viscous fluid. J. Eng. Math. **3**(1), 29–44 (1969). https://doi.org/10.1007/BF01540828
29. K.H. Jeong, M.J. Jhung, Added mass estimation of square sections coupled with a liquid using finite element method. Nucl. Eng. Tech. **49**, 234–244 (2017). https://doi.org/10.1016/j.net.2016.07.010
30. P. Ray, S. Han, A simple and accurate added mass model for hydrodynamic fluid structure interaction analysis. J. Frank. Inst. **6**, 929–945 (1996). https://doi.org/10.1016/0016-0032(96)00043-9

31. H. Y. Lee, S. K. Son, M. G. Won et al., Risks of non-conservative design according to ASME B31.1 for high-temperature piping subjected to long-term operation in the creep range. Nucl. Sci. Tech. 30:77 (2019). https://doi.org/10.1007/s41365-019-0604-4

32. X.Y. Wang, S.F. Zhu, X. Wang et al., Stress and thickness calculation of a bolted flat cover with double metal sealing rings. Nucl. Sci. Tech. **29**, 120 (2018). https://doi.org/10.1007/s41365-018-0457-2